Dissolution kinetics and mechanisms of calcium aluminate inclusions in CaO-Al_2O_3-SiO_2-(MgO) steelmaking slags

Wang, Guang; Nabeel, Muhammad; Dogan, Neslihan; Mu, Wangzhong; Phillion, A. B.

DOI
10.1016/j.ceramint.2025.06.445

Publication date
2025

Document Version
Final published version

Published in
Ceramics International

Ceramics International 51 (2025) 42315–42326

Contents lists available at ScienceDirect

Ceramics International

journal homepage: www.elsevier.com/locate/ceramint

Dissolution kinetics and mechanisms of calcium aluminate inclusions in $CaO-Al_2O_3-SiO_2-(MgO)$ steelmaking slags

Guang Wang [a,*], Muhammad Nabeel [a], Neslihan Dogan [a,b,**], Wangzhong Mu [c,d], A.B. Phillion [a]

[a] Department of Materials Science and Engineering, McMaster University, Hamilton, L8S4L7, Ontario, Canada
[b] Department of Materials Science and Engineering, Delft University of Technology, Mekelweg 2628CD, Delft, the Netherlands
[c] Department of Materials Science and Engineering, KTH Royal Institute of Technology, Brinellvägen 23, 10044, Stockholm, Sweden
[d] Engineering Materials, Department of Engineering Science and Mathematics, Luleå University of Technology, 97187, Luleå, Sweden

ARTICLE INFO

Handling Editor: Dr P. Vincenzini

Keywords:
Dissolution mechanisms and kinetics
Solid calcium aluminate inclusions
In-situ observation
Refractory
Slag viscosity
Clean steel

ABSTRACT

The dissolution kinetics and mechanisms of solid calcium aluminate inclusions ($CaO•2Al_2O_3$ (CA2) and $CaO•6Al_2O_3$ (CA6)) in $CaO-Al_2O_3-SiO_2-(MgO)$ metallurgical slags at 1550 °C were investigated using high temperature confocal laser scanning microscopy (HT-CLSM). The effects of slag viscosity, CaO/Al_2O_3 (C/A) ratio, and MgO content on the dissolution time of CA6 and slag MgO content on that of CA2 particles were examined by tracking the time dependent changes of particle projection areas. The obtained results showed that the dissolution kinetics of CA2 and CA6 particles was enhanced by an increase in slag MgO content. Moreover, increasing C/A ratio of slag or decreasing slag viscosity improved the dissolution rate of CA6 particles. Post dissolution analysis using scanning electron microscopy equipped with energy dispersive X-ray spectroscopy (SEM-EDS) combined with thermodynamic calculations revealed the dissolution paths of CA6 particles in slag S3 with C/A ratio 3.8 and S6 with 8.0 wt% MgO, where the dissolution time is out of expectation. It was found that an intermediate solid layer melilite formed around the undissolved CA6 particle in slag S3 with C/A ratio 3.8, reducing its dissolution rate. Conversely, the formation of randomly dispersed intermediate solid products around the undissolved CA6 particle in slag S6 with 8 wt% MgO did not impend their dissolution rate. Finally, based on the obtained findings, two distinct dissolution mechanisms were proposed advancing the understanding of solid inclusion dissolution in metallurgical slags. The findings obtained from this study aim to provide new insights to further improve steel cleanliness for a longevity of the product service life.

1. Introduction

Steel cleanliness significantly affects the production efficiency and the properties of steels, where the size, number, shape, and composition of non-metallic inclusions (NMIs) are critical factors [1]. Unfortunately, NMIs inevitably form during the secondary steelmaking due to deoxidation and calcium treatment during the ladle furnace (LF) refining process, reoxidation between steel and slag, containers or atmosphere, and erosion and/or corrosion of refractory materials [2]. Inadequate calcium additions during calcium treatment, used to modify irregularly shaped solid alumina-based NMIs to liquid or semi-liquid calcium aluminates with more spherical morphology, can lead to the formation of endogenous solid calcium aluminate NMIs [1,3]. Erosion and corrosion of the refractory lining by the molten slag and steel can result in the formation of exogenous calcium aluminate NMIs, especially for those incorporated with solid calcium aluminates to improve their thermal shock resistance and extend their service life [4–6]. Both endogenous and exogenous NMIs detrimentally affect steel cleanliness and can also hinder steel castability by causing submerge entry nozzle clogging.

During secondary steelmaking, most NMIs are removed by dissolution into the molten slag after floating to the liquid steel – slag interface [7,8]. Rapid dissolution kinetics are crucial to prevent re-entrainment into molten steel and/or clustering within the submerged entry nozzle [9,10]. Conversely, slow dissolution kinetics is desirable to ensure their longevity and maintain service life as refractory materials. Over the past two decades, high-temperature confocal laser scanning microscopy

* Corresponding author.
** Corresponding author. Department of Materials Science and Engineering, McMaster University, Hamilton L8S4L7, Ontario, Canada.
E-mail addresses: wangg84@mcmaster.ca (G. Wang), n.d.dogan@tudelft.nl (N. Dogan).

https://doi.org/10.1016/j.ceramint.2025.06.445
Received 25 March 2025; Received in revised form 17 June 2025; Accepted 29 June 2025
Available online 30 June 2025

(HT-CLSM) has been developed and extensively used to investigate the dissolution behaviors of solid NMIs under conditions relevant to steelmaking, providing in-situ real-time observation. Studies have investigated the dissolution mechanisms and kinetics of NMIs in various steelmaking slag systems as summarized in [11]. However, only a few studies have examined the effect of slag composition and temperature on dissolution kinetics of complex calcium aluminates, particularly $CaO{\bullet}2Al_2O_3$ (CA2). Miao et al. [12] reported that higher temperature and lower SiO_2 content in the slag increased the dissolution rate of CA2 particles. Wang et al. [13] reported that the dissolution kinetics of CA2 particles was enhanced with increasing temperature and slag CaO/Al_2O_3 ratio, as well as decreasing slag viscosity. However, the formation of a melilite layer around CA2 particle hindered its dissolution in slag with CaO/Al_2O_3 ratio of 3.8 at 1550 °C [13]. Guo et al. [14] observed that an increase in MgO content in slag decreased the dissolution time of CA2 particles. Despite those findings, to the best of the current authors' knowledge, no studies have reported the dissolution kinetics and mechanisms of CA6 particles in $CaO\text{-}Al_2O_3\text{-}SiO_2$-(MgO) slag system in the open literature.

Previous studies have shown that intermediate solid products can either accelerate or hinder dissolution. For instance, Park et al. [15] found that CA2 and CA6 formation in the $CaO\text{-}Al_2O_3\text{-}SiO_2$ type slags did not retard Al_2O_3 particles' dissolution rate, whereas the formation of a ring-like layer of $MgO{\bullet}Al_2O_3$ and $2CaO{\bullet}SiO_2$ slowed MgO particles dissolution. Similarly, Guo et al. [16] reported that the formation of a ($2CaO{\bullet}SiO_2$) layer impeded CaO particles dissolution in $CaO\text{-}Al_2O_3$--SiO_2-(MgO) slags. Despite these observations of intermediate solid products formation during particles' dissolution, studies on their formation mechanisms and impact—even their common industrial occurrence—remain limited.

A deeper understanding of the dissolution kinetics and mechanisms of CA2 and CA6 NMIs in $CaO\text{-}Al_2O_3\text{-}SiO_2$-(MgO) metallurgical slags is essential, particularly the role of intermediate solid products. In this research, a comprehensive study of the dissolution behavior of CA2 and CA6 particles in eight different $CaO\text{-}Al_2O_3\text{-}SiO_2$-(MgO) metallurgical slags has been investigated at 1550 °C using HT-CLSM. The effects of slag chemistry on the dissolution kinetics of CA2 and CA6 particles were examined by varying the C/A ratio, viscosity, and MgO content of slags. Interrupted dissolution experiments of CA6 particles in two slags were conducted separately, supplemented by post-experiment analyses using SEM-EDS and thermodynamic calculations to reveal the dissolution reactions at the particle – slag interface, paths and mechanisms. The results of this study aim to clarify the dissolution kinetics, reactions, paths, and mechanisms of CA2 and CA6 particles in $CaO\text{-}Al_2O_3\text{-}SiO_2$-(MgO) metallurgical slags and to understand how underlying factors influence their dissolution behaviors. The obtained knowledge will help improve steel cleanliness, production efficiency and the service life of refractories by enabling the design or selection of optimal slag compositions during refining.

2. Methodology

2.1. Material

Reagent-grade powder of $CaCO_3$, CaO, Al_2O_3, SiO_2, and MgO (Alfa Aesar, USA) was used to synthesize calcium aluminates inclusions (CA2 and CA6) and slags. To avoid the effect of moisture, CaO and MgO were roasted in a muffle furnace for 12 h at 1050 °C, while the $CaCO_3$, Al_2O_3, and SiO_2 were dried in an oven for 24 h at 150 °C before use.

Both CA2 and CA6 pellets were prepared by sintering a 100 g mixture of $CaCO_3$ and Al_2O_3 powder in stochiometric amounts at 1600 °C for 24 h under an argon atmosphere, respectively. CA2 particles were obtained from our previous study [13] and detailed descriptions of the powder mixing and sintering are available elsewhere [12]. The same method was employed to produce CA6 particles.

Three regions of sintered CA6 pellet, i.e. the center layer (purple line), middle layer (blue line), and outer layer (black line), were characterized using X-ray diffraction with a Panalytical X'pert diffraction instrument equipped with a cobalt source (wavelength: 1.789 Å). As shown in Fig. 1, the X-ray diffraction peaks of all three layers align well with the standard CA6 peaks [17] (ICSD 202316, red line), with no other phases detected. These results confirm the successful synthesis of high-purity CA6 particles by sintering. Similar findings were made for CA2 particles [13].

Additionally, the porosity of CA2 and CA6 were measured by X-ray computed tomography (XCT) with a ZEISS Xradia 630 Versa system. The average volume fraction of porosity in CA2 and CA6 particles was found to be 0.25 and 0.39, respectively. This difference in porosity arises from their respective melting points: CA6 particles (1833 °C) and CA2 particles (1765 °C) [18]. Since both were synthesized at 1600 °C, the smaller temperature gap between the sintering and melting point of CA2 particle promotes the growth of "grain" in the particle and reduces the pores in the particle, resulting in a lower porosity in the particle. The procedure for carrying out X-ray tomography, and then determining the volume fraction of voids, can be found in [11].

Slag samples were prepared by mixing powders of CaO, Al_2O_3, SiO_2, and MgO in stochiometric amounts based on the designed composition. The mixtures were heated to a temperature, at least 50 °C higher than the theoretical liquidus temperature ($T_{liq.}$ As shown in Table 1) of each slag, in a platinum crucible (70 mL volume) and placed in a Si-Mo rod resistance furnace under air atmosphere. After fully melted, the slag was held isothermally for 4 h to ensure homogenization. The platinum crucible was then removed from the furnace, and molten slag was poured into a steel plate for cooling. Note the $T_{liq.}$ for each slag was calculated using the Equilibrium module of FactSage 8.0 with FToxid database [19].

Eight different slags were prepared, with the composition presented in Table 1. S1, S2, and S3, which have similar SiO_2 contents but different C/A ratios, were used to study the effect of the C/A ratio on the dissolution kinetics of CA6 particles. S4, S5, and S6, with similar SiO_2 content and C/A ratios but varying MgO contents, were used to investigate the influence of MgO content on the dissolution kinetics of CA2 and CA6 particles. Additionally, S8 was designed to further explore the effect of MgO content on the CA2 dissolution kinetics with similar ΔC_{Al2O3} as S4. S1, S4, and S7 were employed to explore the effect of viscosity on the dissolution kinetics of CA6 particles.

The composition of cooled bulk slags except slag S7 was measured using inductively coupled plasma optical emission spectroscopy (ICP-OES). Slag S7 was prepared by melting 0.0063 g MgO powder in 0.1500 g slag S1 at 1600 °C within a platinum crucible (5 mm in diameter and 6 mm in height) using HT-CLSM for 30 min under an argon atmosphere. Its composition was measured via SEM-EDS. The viscosities of all eight

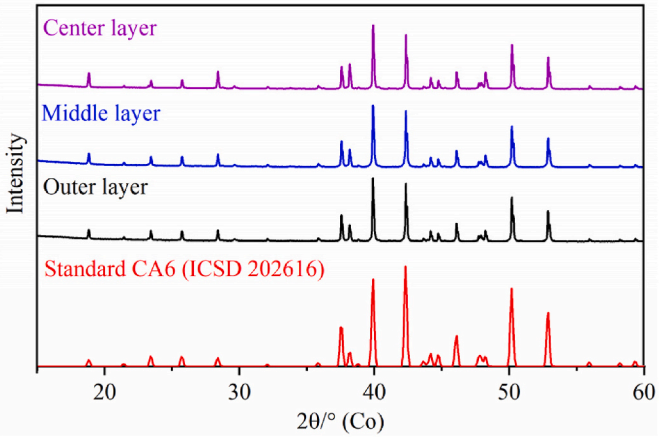

Fig. 1. XRD patterns of the CA6 pellets sintered at 1600 °C under argon atmosphere for 24 h.

Table 1
List of slag composition and properties used in the experiments.

Slag	slag composition wt.%				$T_{liq.}$ (°C)	C/A ratio	μ (Pa.s)	Q	Particle	ΔC_{Al2O3} (kg/m^3)
	CaO	Al_2O_3	SiO_2	MgO						
S1	28.9	31.8	39.3	0.0	1500	0.9	4.4	3.7	CA6	606
S2	38.3	20.7	41.1	0.0	1305	1.8	2.8	3.1	CA6	887
S3	49.1	13.0	37.9	0.0	1440	3.8	1.2	2.3	CA6	372
S4	48.0	36.0	16.0	0.0	1509	1.3	0.9	3.0	CA2	694
									CA6	227
S5	45.4	34.4	16.3	4.0	1450	1.3	0.8	2.8	CA2	819
									CA6	707
S6	43.3	32.7	16.1	8.0	1526	1.3	0.7	2.6	CA2	959
									CA6	114
S7	27.6	30.8	37.6	4.0	1405	0.9	3.3	3.5	CA6	521
S8	39.5	44.1	8.5	8.0	1524	0.9	0.7	3.1	CA2	688

slags were calculated using Urbain model [20], which has been widely employed to determine the viscosity of steelmaking slags based on the function of each oxide component on the slag structures.

2.2. Experimental procedure

An HT-CLSM (VL2000DX-SVF17SP, Yonekura) was used to carry out the CA2 and CA6 particles dissolution and interrupted experiments, enabling continuous in-situ observation. Technical details and operation procedures for the HT-CLSM facility are available elsewhere [21,22]. The CA2 and/or CA6 particle dissolution experiments were conducted as follows: approximately 0.15 g of slag was pre-melted in a platinum crucible (5 mm in diameter and 6 mm in height) within the HT-CLSM furnace. A CA2 or CA6 particle was then placed on top of the pre-melted slag, and the assembly was heated to the experimental temperature according to a specified heating profile. High purity Argon gas (99.999 %) was purged into the furnace with a flow rate 20 mL/min (cc) throughout the dissolution experiment. The entire dissolution process of the CA2 and CA6 particles was recorded in real-time using a CCD camera at a frame rate of 5 Hz. It should be noted that the mass of the CA2 or CA6 particle used in each dissolution experiment is less than 0.1 wt% of that of slag to avoid changing slag composition and properties. Post-experimentation, the ImageJ [23] software was used to measure the changes in the projection area (A) of the dissolving CA2 and CA6 particles. A was measured manually based on the contrast difference between the particle and molten slag. Each image was measured three times, and the average values were reported.

Fig. 2 illustrates the schematization of the sample setup and the heating profile. The CA2 or CA6 particle and platinum crucible containing pre-melted slag were placed in an alumina crucible positioned on a sample holder. A B-type thermocouple at the base monitored the temperature (Fig. 2(a)). Each dissolution experiment followed the same heating profile (Fig. 2(b)), including a rapid heating rate of 1000 °C/min to 1500 °C, followed by 50 °C/min until reaching the test temperature of 1550 °C. The start time of dissolution, t_0, was defined as when the CA2 or CA6 particle was seen to be fully immersed into the molten slag at the test temperature. The experiment continued until the particle had fully dissolved.

Interrupted dissolution experiments were performed on three CA6 particles in slag: S3 after 60 s and 600 s, and S6 after 10 s, respectively. The system was then quenched using helium (Fig. 2(b)). The samples obtained from the interrupted experiments were grounded and polished for electron microscopy. SEM-EDS analysis (with carbon coating, 15 nm thickness) was performed using a JEOL 6610 LV to characterize the CA6 particle – slag interface.

3. Results and discussions

This section begins with the thermodynamical analysis of CA2 and CA6 particles dissolution in slags at 1550 °C using the Phase Diagram

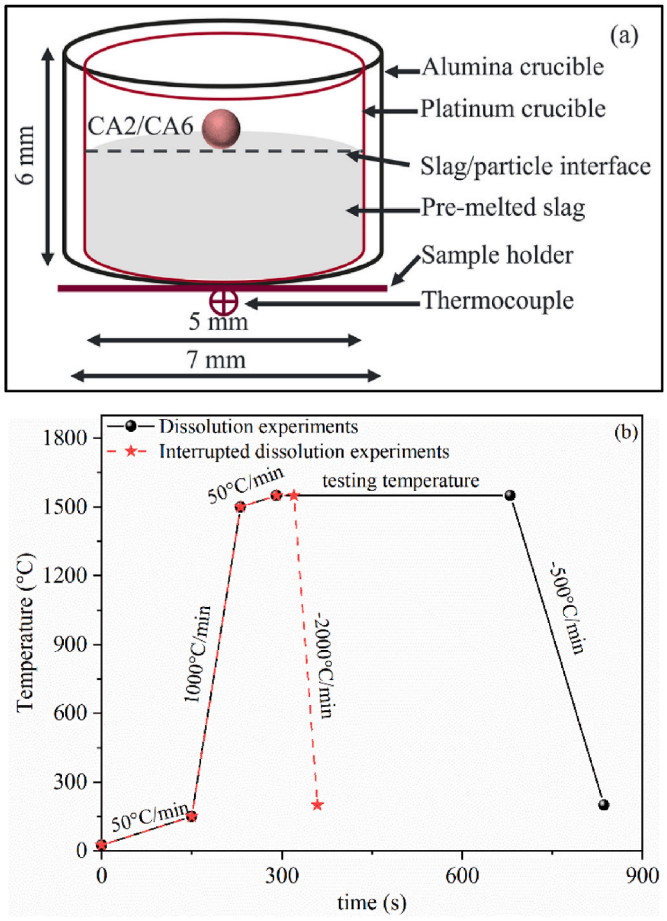

Fig. 2. Schematic illustration of (a) sample setup and (b) the heating profiles used in dissolution and interrupted experiments.

module of FactSage 8.0 with FToxid database [19]. The objective of Section 3.1 is to better understand the influence of slag composition on the dissolution paths of CA2 and CA6 particles and predict potential stable phases. Section 3.2 provides experimental results on the impacts of slag viscosity, C/A ratio, and MgO content on the dissolution kinetics of CA2 and CA6 particles. The underlying mechanisms of these effects are analyzed and discussed. In Section 3.3, the dissolution paths of CA6 in slag S3 and S6 are determined. A comparison of the dissolution paths between the thermodynamic predictions (calculations) and the experimental observations incorporating SEM-EDS analysis of particle – slag interface is presented, providing the formation mechanisms of the intermediate solid products. Building on both thermodynamic predictions and experimental results, Section 3.4 proposes two different dissolution

mechanisms of solid particles and evaluates their impact on the dissolution kinetics. Finally, Section 3.5 provides a brief discussion on slag selection considerations for optimizing NMIs removal while balancing refractory service life.

3.1. Thermodynamics analysis

Fig. 3 compares the phase changes with respect to MgO content in slag phase, including the ternary phase diagram for CaO-Al_2O_3-SiO_2 (Fig. 3(a)), the pseudo-quaternary phase diagram 4 wt% MgO-CaO-Al_2O_3-SiO_2 (Fig. 3(b)) and 8 wt% MgO-CaO-Al_2O_3-SiO_2 (Fig. 3(c)). These diagrams highlight the compositions of CA2 and CA6 particles, the initial compositions of the eight slag groups, and potential phase zones. Additionally, black solid lines represent two-phase tie lines, while red dashed and solid arrows denote the expected dissolution paths of CA2 and CA6 particles in the eight slags.

Although the particle dissolution is inherently a non-equilibrium process and the dissolution path may not follow a straight trajectory, the phase diagrams provide valuable insights into the phases that may precipitate near the CA2 and CA6 particles during dissolution. Notably, the initial compositions of all eight slags are located within the fully liquid region of the phase diagrams, as shown in Fig. 3.

Fig. 3(a) presents the expected dissolution paths of CA6 particles in slag S1 - S4 and CA2 particles in slag S4. The expected dissolution paths of CA6 particles in slag S1 and S2 do not intersect phase zones a_2 or a_3, suggesting that no intermediate solid products are likely to form. Conversely, the dissolution paths of CA2 and CA6 particles in slags S3 and S4 traverse the phase zone containing melilite, suggesting potential precipitation on the particle surface.

Fig. 3(b) depicts the expected dissolution paths for CA6 particles in slag S5 and S7, and the dissolution path of CA2 particles in slag S5. For the dissolution of CA2 particles in slag S5, the dissolution path crosses phase zones b_2 and b_3, predicting the formation of intermediate product like spinel (MA). Similarly, for CA6 particles in slag S5 and S7, the intermediate solid products like $2CaO•2MgO•14Al_2O_3$ (C2M2A14), $CaO•2MgO•8Al_2O_3$ (CM2A8), and MA are expected to form.

Fig. 3(c) illustrates the dissolution path of CA6 particles in slag S6 and CA2 particles in slag S6 and S8. For CA6 particles in slag S6, similar intermediate solid products (CA2, CM2A8, and MA) are expected as in slag S7. For CA2 particles, MA is the only predicted intermediate solid product in slag S6 and S8.

Generally, the formation of an intermediate solid product layer on the surface of a solid particle can impede the dissolution of particles by retarding the transport of products from and reactants to the particle surface [24]. Moreover, the formation of intermediate solid layer around the undissolved particle would decrease the concentration difference (ΔC) of the dissolving species by changing the bulk slag and the particle – slag interface to solid product layer – slag interface, thereby reducing the ΔC for dissolution compared to systems without intermediate solid layer formation [16]. In the present study, the ΔC for CA2 and CA6 particles dissolution is assumed to be the concentration difference between the bulk slag and the saturation content for Al_2O_3 ($\Delta C_{Al_2O_3}$). This assumption is supported by the significantly small size and higher diffusion coefficient of Ca^{2+} cation compared to AlO_x^{y-} anion [25].

3.2. Dissolution kinetics parametric study

3.2.1. Effect of slag viscosity on the dissolution kinetics of CA6 particles

The influence of slag viscosity on the dissolution kinetics of CA6 was examined using slags, S1, S7, and S5, with similar $\Delta C_{Al_2O_3}$ and slag C/A ratio but varying slag viscosities. In slag S1 and S7, CA6 particles exhibited slow motion during the dissolution process, while in slag S5, the particle moved rapidly.

It is well known that the slag viscosity strongly relates to its structure at molten status. Polymer- and structure-based theories [26] suggest

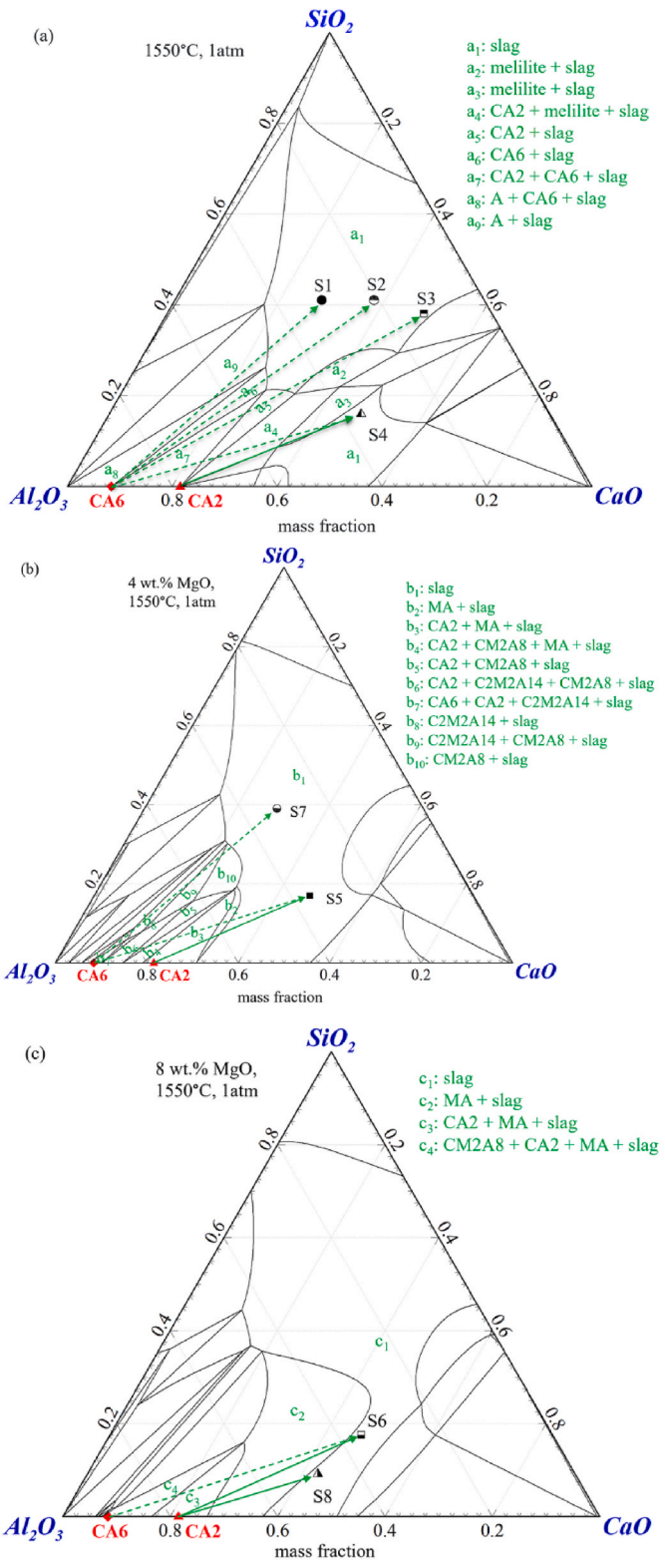

Fig. 3. Prediction of phase stability of the CA2 and CA6 particles – CaO-Al_2O_3-SiO_2 based slag systems at 1550 °C, (a) slag without MgO, (b) slag with 4 wt% MgO, and (c) slag with 8 wt% MgO. Dash and solid arrows represent the dissolution path of CA6 and CA2 particles, respectively. (C: CaO, A: Al_2O_3, S: SiO_2, M: MgO).

that the types and quantities of oxides influence the structure of slag, as these can function as either network formers or breakers. Slag oxides are typically classified into three categories. The first category, "acid oxides, " such as SiO_2, forms complex three-dimensional networks of anionic complexes. The second category, "basic oxides," including CaO and MgO, disrupt these networks. The third category, "amphoteric oxides," exemplified by Al_2O_3, exhibits behavior that varies depending on the slag composition and lacks a distinct categorization [26,27].

To quantitatively describe the slag structure, the parameter *Q*, i.e. the degree of slag polymerization, was developed [25]. A higher *Q* value denotes that the structural unit within the slag is larger, leading to higher resistance for dissolving species transport in this molten slag. Decreasing the *Q* value from 4 to 0 is known to modify the slag structural unit from a 3D tetrahedra to a monomer [25]. For the CaO-Al_2O_3--SiO_2-MgO slag system, *Q* can be calculated using the following equations [25]:

$$Q = 4 - NBO/X_T \tag{1}$$

$$NBO = 2\left(X_{CaO} + X_{MgO} - 2X_{Al_2O_3}\right) \tag{2}$$

$$X_T = X_{SiO_2} + 2X_{Al_2O_3} \tag{3}$$

where *NBO* is the number of non-bridge oxygen atoms, X_T is the number of tetragonally-coordinated atoms, and X_i is the molar ratio of component *i* in the slag. The *Q* values for slag S1, S7, and S5 are 3.7, 3.5, and 2.6, respectively.

Fig. 4 presents the normalized area change of CA6 particles over time. The total dissolution time of CA6 particles decreased from 819 s to 432 s by decreasing the slag viscosity from 4.4 to 3.3 Pa s, coupled with an increase in $\Delta C_{Al_2O_3}$ from 506 kg/m^3 (15.5 wt%) to 521 kg/m^3 (16.1 wt%). With a further decrease in the viscosity to 0.8 Pa s, coupled with an increase in $\Delta C_{Al_2O_3}$ to 707 kg/m^3 (20.5 wt%), the total dissolution time dropped to around 36 s. Moreover, the reduction in *Q* values from 3.7 to 2.6 suggests a transformation in the slag structure from a sheet-like to a chain-like configuration [25]. This transformation decreased the transportation resistance for dissolving species in the molten slag and enhanced particles dissolution, consistent with previous studies [13].

3.2.2. *Effect of C/A ratio on the dissolution kinetics of CA6 particles*

The influence of slag C/A ratio on the dissolution kinetics of CA6 particles was investigated in three slags with C/A ratios 0.9, 1.8, and 3.8, each possessing approximately 40 wt% SiO_2 at 1550 °C. Throughout the dissolution process, CA6 particles exhibited slow motion in all three slags.

Fig. 5 shows the normalized area change of CA6 particles with time. The total dissolution time of CA6 particles was initially dropped from 819 s to 174 s by increasing the C/A ratio from 0.9 to 1.8. This decrease can be attributed to a reduction in slag viscosity from 4.4 to 2.8 Pa s and a decrease in *Q* from 3.7 to 3.1, coupled with an increase in $\Delta C_{Al_2O_3}$ from 506 kg/m^3 (15.5 wt%) to 912 kg/m^3 (28.7 wt%). However, with a further increase in the C/A ratio to 3.8, the total dissolution time unexpectedly increased to 1001 s despite a further reduction in slag viscosity and *Q* to 1.2 Pa s and 2.3, respectively. This suggests that although the resistance was lower for the transportation of the dissolving species in this slag, the change in the slag structure, from a sheet-like to a chain-like structure, may have altered the dissolution behavior. [25]. Even though there is a drop in $\Delta C_{Al_2O_3}$ to 793 kg/m^3 (26.5 wt%), this increase is likely due to the potential formation of intermediate solid product melilite, as predicted by the phase diagram in Section 3.1. Similar dissolution behaviors have been reported by the current authors [13] for the dissolution of CA2 particles in those three slags at 1550 °C.

3.2.3. *Effect of MgO content on dissolution kinetics of CA2 and CA6 particles*

The influence of MgO content on the dissolution kinetics of CA2 and CA6 particles was analyzed at 1550 °C in three slags with MgO content of 0, 4, and 8 wt%. Those slags had a similar C/A ratio of 1.32 and a similar SiO_2 content of 16 %.

Fig. 6 illustrates the normalized area change of CA2 particles as a function of time. The total dissolution time of CA2 particles decreased from 47 s to 17 s with an increase of MgO content from 0 (slag S4) to 8 wt % (slag S6). This trend is attributed to the combined effects of an increase in $\Delta C_{Al_2O_3}$ from 694 kg/m^3 (19.7 wt%) to 959 kg/m^3 (27.0 wt%), a reduction in slag viscosity from 0.9 to 0.7 Pa s, and a decrease in *Q* from 2.97 to 2.56.

Slag S8 with 8 wt% MgO (red circle in Fig. 6) and slag S4 without MgO (solid red circle in Fig. 6), had similar $\Delta C_{Al_2O_3}$ (690 kg/m^3), were compared to examine the specific influence of MgO content on the dissolution kinetics of CA2 particles. Additionally, the *Q* values are comparable for S4 (3.0) and S8 (3.1). The total dissolution time of CA2 particles decreased from 47 s to 22 s by increasing the MgO content from 0 to 8 wt%. The slight reduction in slag viscosity from 0.9 to 0.7 Pa s is unlikely to contribute this improvement. By comparing the dissolution

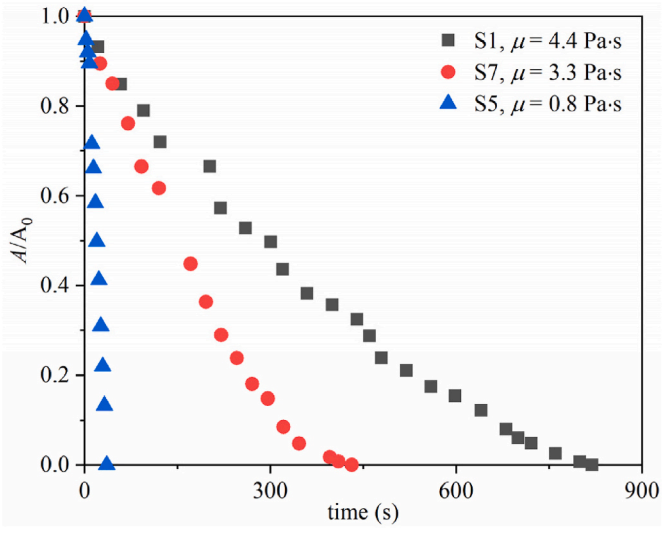

Fig. 4. Normalized area changes of CA6 particles as a function dissolution time at 1550 °C in slags with different viscosities.

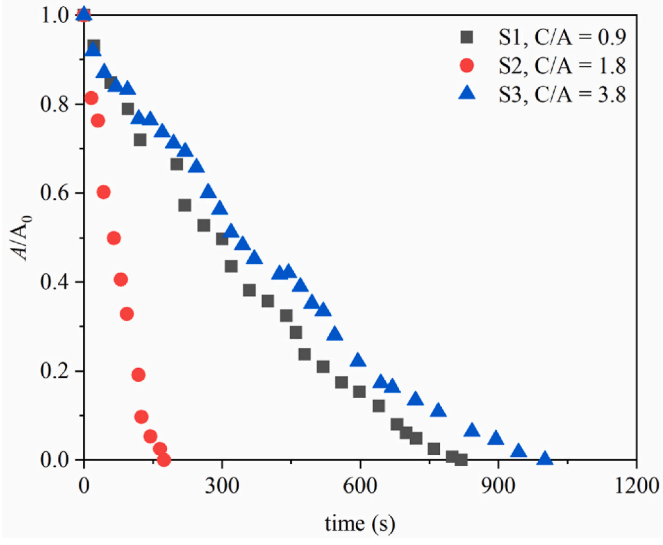

Fig. 5. Normalized area changes of CA6 particles as a function of time at 1550 °C in slags with different C/A ratios.

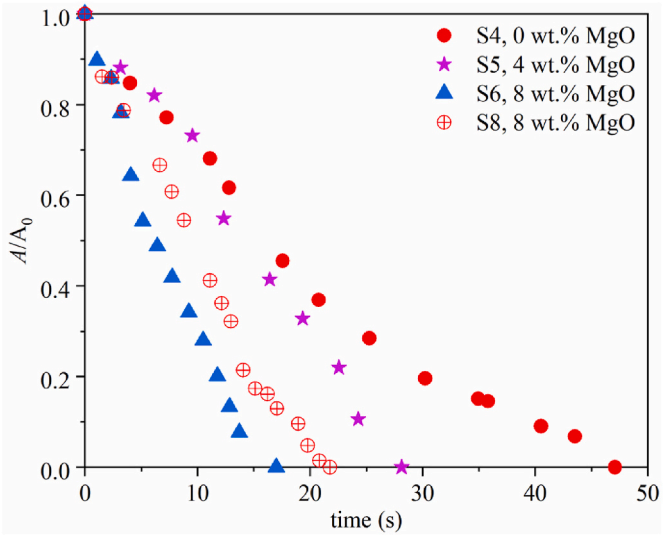

Fig. 6. The normalized area changes of CA2 particles as a function dissolution time at 1550 °C in slags S4-S6 with different MgO contents but same C/A ratio, slags S4 and S8 with different MgO contents but similar ΔC_{Al2O3}.

paths of CA2 particles in slags S4 and S8, shown in Fig. 3(a) and (c), it is seen that the intermediate solid product MA only forms during CA2 particle dissolution in slag S8. The current authors claim that the formation of MA phase positively impact the dissolution kinetics, contrasting the role of melilite in slag S3 for CA2 dissolution reported in [13]. This comparison suggests the formation of intermediate solid products might have different impacts on the dissolution kinetics of particles. More discussions were given in Section 3.4.

CA6 particles moved and rotated in all three molten slags during the dissolution process. Fig. 7 shows the normalized area change of CA6 as a function of time for slags with varying MgO contents. The total dissolution time of CA6 decreased from ~49 s to ~36 s as the MgO content increased from 0 to 4 wt%, due to the increase of $\Delta C_{Al_2O_3}$ (229 kg/m^3 (6.8 wt%) to 707 kg/m^3 (20.5 wt%)), combined with a slight decrease in slag viscosity from 0.9 to 0.8 Pa s and a decrease in Q from 3.0 to 2.8. Further increase in the MgO content to 8 wt%, the dissolution time further decreased to 24 s. At this MgO content, the slag viscosity and Q were slightly decreased to 0.7 Pa s and 2.6, respectively, while the $\Delta C_{Al_2O_3}$ dropped to 114 kg/m^3 (3.6 wt%). Moreover, an examination of the dissolution pathways indicated that the intermediate solid products were expected to form during CA6 dissolution in all three slags, as detailed in Section 3.1. This behavior suggests that factors, such as the formation of intermediate solid products, beyond $\Delta C_{Al_2O_3}$ and slag viscosity may influence the dissolution kinetics of the CA6 particles at high MgO content, or the formation of intermediate solid products might affect the prediction of $\Delta C_{Al_2O_3}$ using FactSage 8.0 [19]. More discussions were given in the following sub-section.

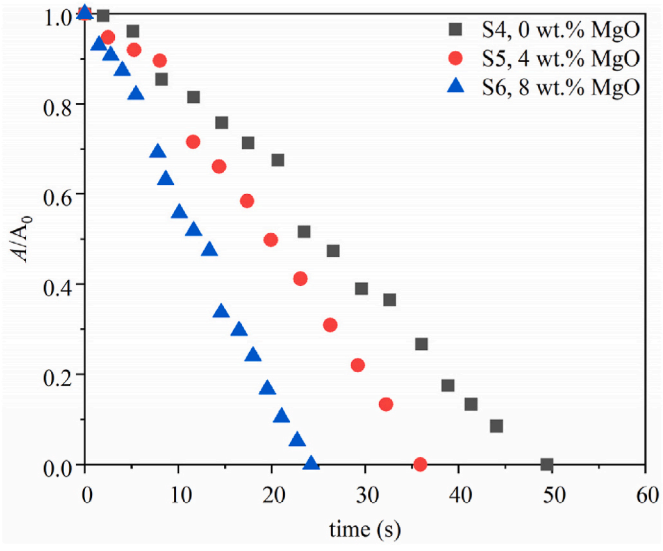

Fig. 7. The normalized area changes of CA6 particles as a function dissolution time at 1550 °C in slags with different MgO contents.

3.3. Determination of dissolution path

To gain deeper insights into the impact of the dissolution path of CA2 and CA6 particles on the dissolution kinetics, the interrupted dissolution experiments for CA6 particles were performed in slag S3 after 60 s and 600 s, and in slag S6 after 10 s dissolution, respectively. SEM-EDS analysis was conducted along the CA6 particle – slag interface, and the results were analyzed in conjunction with thermodynamic calculations using FactSage 8.0 [19]. The results are presented in Figs. 8–11. Moreover, the potential chemical reactions forming the intermediate solid products, indicated by phase diagrams and SEM-EDS results, during those dissolution processes were obtained using Reaction module of FactSage 8.0 with FToxid database [19], as listed in Table 2. From the thermodynamic point view, the free Gibbs energy of each reaction at 1550 °C is negative, indicating all those reactions can happen at experimental conditions. It also can be found that the reaction constant, K_{eq}, at equilibrium condition for Reactions (2), (4–6), and (8–10) is much greater than that of Reactions (1), (3) and (7), showing Reactions (2), (4–6), and (8–10) are much faster compared to that of Reactions 1, 3 and 7 under the same experimental conditions.

Fig. 8(a) shows the in-situ image of the CA6 particle dissolving in slag S3 at 1550 °C after 600 s. The undissolved particle is outlined by a red dash boundary. A surrounding layer, visible between the solid black line and red dash line, exhibits a semi-transparent appearance distinct from the opaque undissolved particle. This indicates the formation of a new product layer during the dissolution process. A similar phenomenon has been reported by Liu et al. [10] for the dissolution of MgO particle in 29.9CaO-23.5Al_2O_3-39.3SiO_2-7.3MgO (wt.%) slag at 1600 °C. Additionally, gas bubbles are visible on the surface of the undissolved particle, likely resulting from air trapped within the pores of the CA6 particle.

Fig. 8(b) illustrates the SEM backscattered electron image of the CA6 particle – slag S3 interface after 600 s dissolution, highlighting three distinct regions based on variations in contrast and line scan results (Fig. 9(c)). The white region beyond the solid black line corresponds to slag S3, the gray region between the solid black line and the red dashed line represents the intermediate solid product layer melilite, and the dark gray region within the red dashed boundary contains a mixture of undissolved CA6 particle, melilite, CA2 and slag. These features align well with the morphology observed in the in-situ image (Fig. 8(a)). The apparent shape difference between the particle in the in-situ image and the SEM image arises from the projection area captured in the in-situ image, while the SEM image reflects the actual cross-sectional shape after polishing. Note that in some circumstances, over-polishing can lead to shape alterations in the sample.

To provide a clearer view of the interface, a localized area spanning the three regions, marked by a white dashed boundary in Fig. 8(b), was magnified to 1000× (Fig. 8(c)). The magnified image distinctly highlights the color differences between the regions, revealing gray areas within the black region. The SEM-EDS point analysis, presented in Table 3, indicates that spectra 1 and 3 in the white region match the elemental composition of slag S3, confirming it as the bulk slag. The gray regions (spectra 2, 4–6, and 10) align with the composition of melilite, while spectra 8 and 11 in the black region correspond to the CA2 phase. Moreover, spectra 7 and 9 in the light black region indicate a mixture of

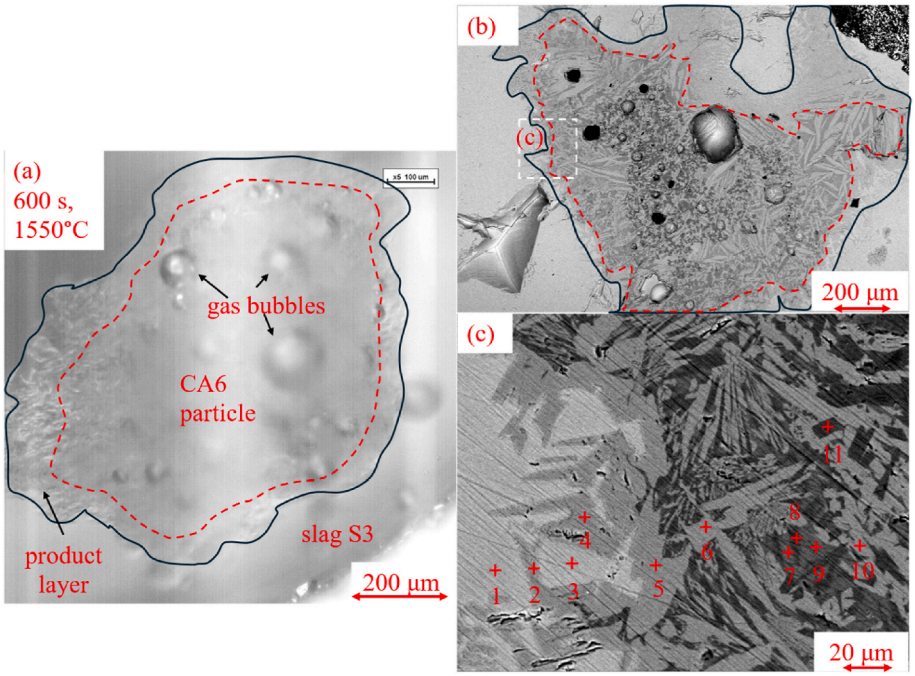

Fig. 8. Images showing the formation of distinct phases during CA6 particle dissolution in slag S3 at 1550 °C after 600 s. (a) in-situ image, and (b–c) SEM back scattered electron images.

these phases. The results suggested that molten slag, penetrated through the pores of CA6, formed new phases of melilite and CA2 through Reactions 1–4.

To accurately interpret the line scan results and with respect to the dissolution path, a systematic approach was employed to distinguish between the CA6 particle, slags (S3, S6), and intermediate solid products (C2AS (melilite), CA2, MA, and CM2A8). Each of these compounds has a distinct elemental composition, as summarized in Table 4. Thus, the SEM-EDS line scan data along the particle – slag interface were compared with the theoretical compositions of those potential compounds. Regions along the scanned line were identified as particle, slag, intermediate solid products or mixture based on their elemental composition. For example, in the CA6 particle – slag S3 system, the non-Si regions, with Al and Ca constituting ~48 and ~6 wt% at the particle – slag interface, can be classified as CA6, while regions where Ca, Al, and Si coexist, with Ca, Al and Si constituting ~30, ~20 and ~10 wt%, can be identified as melilite. Boundary layers are regions having a decreasing Ca and Si composition while the Al content steadily increases. The regions where Ca, Al, and Si coexist, with Ca and Si constituting ~34 and ~17 wt% can be classified as slag S3. The other regions can be considered as mixtures.

Fig. 9 presents the SEM backscattered electron image, and the elements Ca, Al, and Si distribution obtained from the EDS line scan of the CA6 particle – slag S3 interface after 60 s (Fig. 9(a) and (b)) and 600 s (Fig. 9(c)) of dissolution at 1550 °C, respectively. Following the defined criteria, different regions were identified. In Fig. 9(a), the dark-gray region in the center of SEM image presented undissolved CA6 particle whereas light gray outer region was slag S3. New phases, such as CA2 and melilite, were identified between these two regions. This finding is in good agreement with the thermodynamic predictions shown in Fig. 3 (a). Due to relatively high porosity of the CA6 particle, slag S3 was able to penetrate towards the core of particle through the pores. No boundary layer observed between the intermediate solid products and the undissolved particle, indicating the mass transfer of the dissolving species through the intermediate solid layer was not the rate-limiting step for CA6 particle dissolution. However, a boundary layer between slag S3 and the melilite was identified in Fig. 9(a), though not clearly visible due to the long scan distance. To clarify this, a localized short line scan along the slag S3 – melilite layer was conducted (Fig. 9(b)), revealing a distinct boundary layer based on the Al and Si contents distribution. Interestingly, the Al content initially increased, then dopped to a content lower than that in the bulk slag before rising to match that of melilite, while the Si content increased before decreasing to a content similar as that in the melilite. This differs from the continuous elements distribution trend observed for CA2 particle dissolution in 30.5CaO-23.2Al_2O_3-46.3SiO_2 (wt.%) slag [12], and Al_2O_3 particle dissolution in CaO-MgO-SiO_2-Al_2O_3-TiO_2 slags [28]. The observed Al drop at the melilite – boundary layer interface is likely due to the growth of melilite on this side by consuming Al, which results in Si enrichment.

A similar trend was observed for CA6 particle in slag 3 after 600 s dissolution, as shown in Fig. 9(c). However, the average thickness of melilite layer is noticeably thicker compared to that observed after 60 s dissolution, suggesting its accumulation over time during the dissolution process. It is important to note that the CA2 and CA6 regions primarily consist of CA2 and CA6, respectively, but also contain minor amounts of other phases due to the penetration of molten slag through the pores.

In summary, SEM-EDS analysis confirmed that the formation of a new intermediate solid phase as predicted by the thermodynamic calculations is melilite, presented in the form of solid layer. This solid layer around the undissolved particle reduced the dissolution rate of CA6 particle in slag S3 by inhibiting the transport of species and reducing $\Delta C_{Al_2O_3}$ by altering the interface from slag – particle to slag – intermediate solid layer, significantly slowing dissolution kinetics.

Fig. 10(a) shows the in-situ image of CA6 particle dissolved in slag S6 at 1550 °C after 10 s. The region enclosed by the red dash boundary represents the undissolved particle. Surrounding this, a distinct layer can be observed between the solid black line, which is suggested to be the boundary layer by the line scan results in Fig. 11. In addition, gas bubbles were observed on the surface of the undissolved particle, likely resulting from air trapped in the particle pores.

As shown in Fig. 10(b), the interface between the CA6 particle and slag S6 after 10 s of dissolution at 1550 °C can be divided into three distinct regions based on SEM backscattered imaging and EDS analysis: the white region outside the solid black line corresponds to slag S6, the gray region between the solid black line and red dashed line represents the boundary layer, and the light black region enclosed by the red

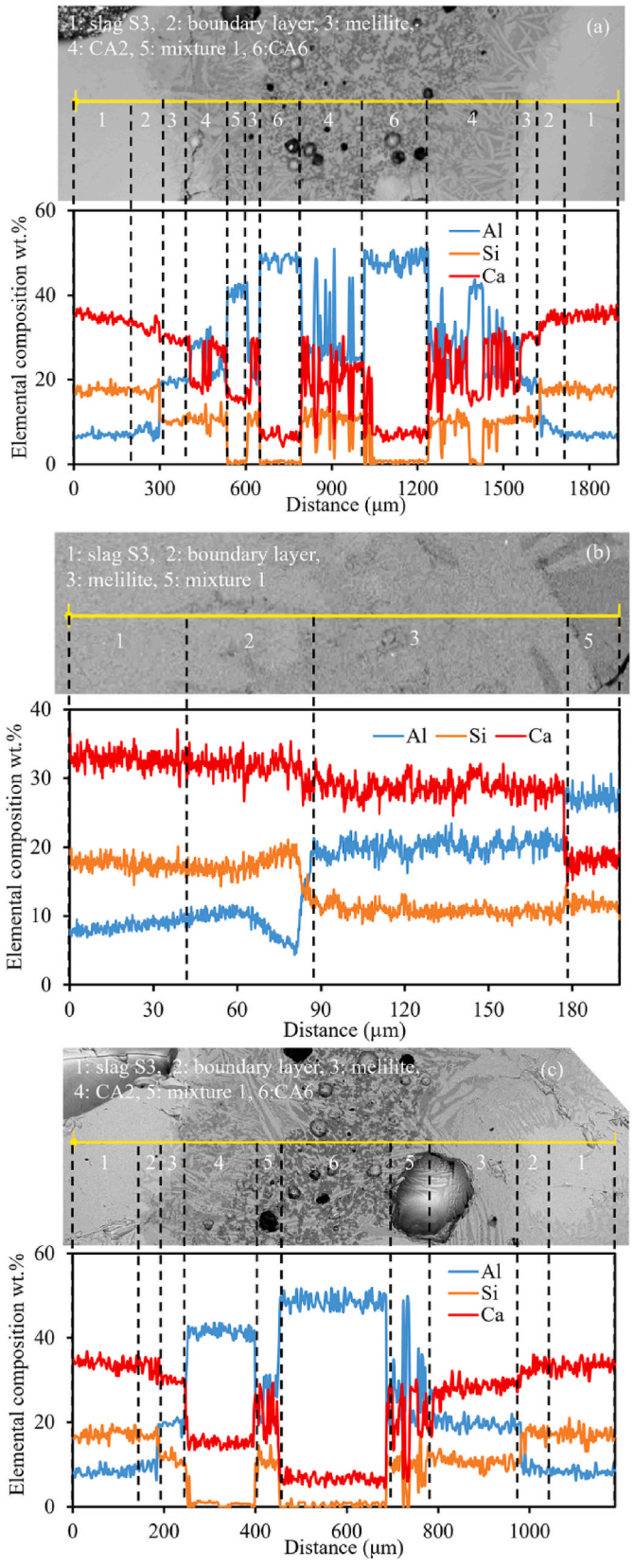

Fig. 9. SEM backscattered electron image and EDS line scan analysis of CA6 particle – S3 slag interface (a) through the entire undissolved particle and (b) at the slag – product layer interface after 60 s dissolution, respectively, and (c) through the entire undissolved particle after 600 s dissolution at 1550 °C. Mixture 1 contains CA6 + CA2 + melilite + slag S3.

dashed line denotes the undissolved particle.

SEM-EDS points and map scans were conducted on magnified areas crossing these regions (Fig. 10(c) and (d)). The point scan results (Fig. 10 (c)–Table 5) show that spectra 2, 8, 10, and 11 align with the elemental composition of CA6, confirming that the dark regions are undissolved CA6 phase. Adjacent spectra, such as points 1, 7, and 9, match the CA2 phase composition, indicating the formation of CA2 as a reaction product of CA6 with slag S6 (via Reactions (1) and (2)). In addition, spectra 3 and 4 identify MA in the deep black regions near the CA2 phase, formed through Reactions (8) and (10). Further analysis reveals that spectra 5, 6, and 12 correspond to a mixture of molten slag and potential solid products, while spectra 13 and 14 in the outermost region confirm the presence of slag S6. Notably, CM2A8 phase was not detected, possibly due to (a) its content being below the detection limit or (b) its rapid consumption through subsequent Reaction (10). The SEM-EDS map scan of another region (Fig. 10(e)) further corroborates these findings. The elemental distributions observed in the map scan confirm the compositions and spatial arrangements of CA6, CA2, MA, and slag S6, consistent with the results of point and line scans.

To gain deeper insight into the dissolution mechanism, the SEM-EDS line scan was done along the CA6 particle – slag S6 interface after 10 s of dissolution at 1550 °C. Fig. 11 presents the SEM backscattered electron image, and the elements Ca, Al, Si, and Mg distribution obtained from the line scan, revealing distinct regions along the interface. On the left side of the scanned line, slag S6, followed by a boundary layer of about 80 μm. Beyond this layer, a mixed region is observed, characterized by fluctuations in elemental concentrations and comprising CA6, CA2, MA, and slag S6. This finding aligns well with the points scan results at other regions of this interface.

Based on the above analysis, the dissolution behavior of CA6 particles in slag S6 can be summarized as follows. Initially, a distinct boundary layer formed between the particle and the bulk slag. As slag penetrates through porous CA6 particle, they reacted and produced intermediate solid products of MA, and CA2. These products occurred in small amounts, had a small size, and were randomly dispersed. Due to their small size, the particles didn't obstruct the transport of reactants to the CA6 particle – slag S6 interface, maintaining the slag – particle interface rather than forming a new intermediate solid product – slag interface, unlike the dissolution behavior of CA6 particle determined in slag S3, where the intermediate solid product layer (melilite) formed around the particle. They were considered not to hinder the dissolution of CA6 particles. As a result, the $\Delta C_{Al_2O_3}$ was not affected by the formation of these products on the particle surface. This finding highlights the importance of where the solid products form and clarifies the differences between dissolution experimental results. It also confirmed that the limitation of thermodynamic model prediction on $\Delta C_{Al_2O_3}$, especially for the presence of intermediate solid products.

3.4. Dissolution mechanisms of particles in molten slags

Based on the detailed analysis of CA2 and CA6 particles dissolution in different slags, two distinct dissolution mechanisms have been identified for the dissolution of solid particles, corresponding to three types of behavior schematically illustrated in Fig. 12(a)–(c), as well as the concentration profile of the dissolving species in Fig. 12 (a1) - (c1). The dissolution process can generally be categorized into two types: (1) direct dissolution and (2) indirect dissolution.

In addition to the size evolution, the role of dissolved species diffusion in governing dissolution behavior is considered, as diffusion coefficients can vary depending on slag composition, temperature, and the presence of interfacial reaction products.

3.4.1. Direct dissolution

As shown in Fig. 12(a), the particle dissolves directly into the molten slag, with its size gradually decreasing until it is fully dissolved. A boundary layer forms at the interface once the particle is immersed in

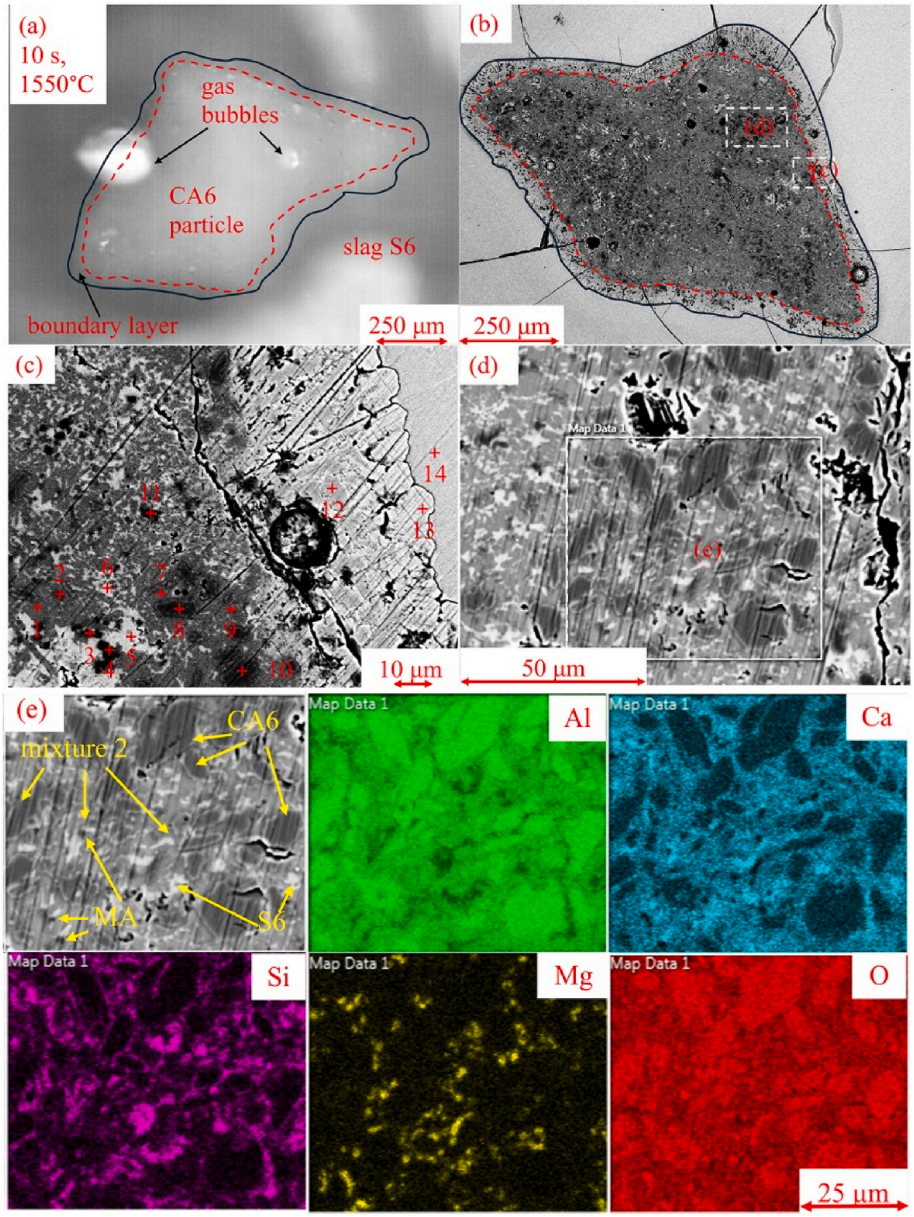

Fig. 10. Images showing the formation of different phases during CA6 particle dissolving in slag S6 at 1550C. (a) in-situ image at 10 s, (b–d) SEM back scattered electron image, and (e) SEM-EDS map scan results.

the molten slag. Reactants and products are transported across this boundary layer, making mass transport through the layer the rate-limiting step. Additionally, the driving force (ΔC) (concentration difference of the dissolving species between the particle – slag interface (C_s) and the bulk slag (C_b)) is constant ($\Delta C = C_s - C_b$) during the dissolution process (Fig. 12(a1)). CA6 particles dissolving in slags S1, S2, and S4 followed this mechanism. In this case, the effective diffusion coefficient of the dissolving species in the molten slag is controlled by the temperature and slag viscosity and the values varied between $1.25*10^{-11}$ and $1.09*10^{-10}$. These values agree with those available in open literature [11,12].

Fig. 12(b) presented the second case of direct dissolution, where intermediate solid products formed during the dissolution process, presented as randomly dispersed and tiny particles around and within the undissolved particle, due to the chemical reactions between the slag and the solid particle, as depicted from t_0 to t_2. Then they dissolved within the slag together with the undissolved particle, as shown from t_1 to t_4. The formation of these types of products has no impact on the ΔC ($C_s - C_b$), as their amount is too small to change the C_b and the interface between solid particle – slag, as shown in Fig. 12(b1). The dissolution of CA2 and CA6 in MgO-containing slags (S5, S6, S7, S8) is expected to result in the formation of intermediate products. The presence of MgO in slags S5–S8 may reduce slag viscosity and enhance ionic mobility, potentially increasing the diffusion coefficients of dissolving species and accelerating overall mass transport. Given that the dissolution occurred more rapidly in the presence of MgO, it can be inferred that the formation of these particles may further consume CA2 and CA6 through additional reactions alongside the dissolution process in the slag. While it would be premature to conclude that dissolution is accelerated by formation of the intermediate particles, they do not impede the dissolution process.

3.4.2. *Indirect dissolution*

Under this mechanism illustrated in Fig. 12(c), once the particle is fully immersed into the slag, the formation rate of intermediate solid products exceeds their dissolution rate. As a result, these products grow

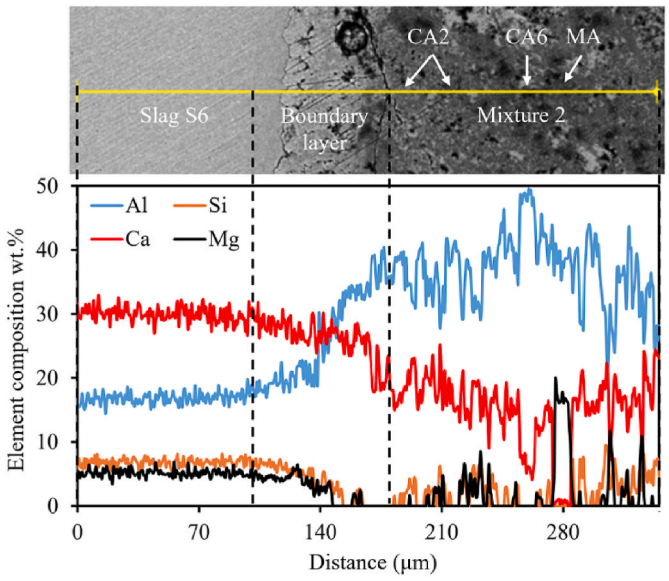

Fig. 11. SEM back scattered electron image and EDS line scan analysis of CA6 particle – slag S6 interface after 10 s dissolution at 1550 °C. Mixture 2 contains CA6 + CA2 + MA + slag S6.

Table 2
A list of potential chemical reactions for the formation of intermediate solid products during CA2 and CA6 particles' dissolution process in molten slags. These reactions are calculated using Reaction module of FactSage 8.0 with FToxid database [19].

	Reactions	$\Delta G = a + bT$ (1573–2273K)	T = 1823 K	
			ΔG (J)	K_{eq}
1	$(CA6)_s + (C)_l = 2(CA2)_s + 2(A)_l$	97,340–90.65T	−432056	17.29
2	$(CA6)_s + 2(C)_l = 3(CA2)_s$	−212,831 + 11.39T	−195375	3.96E5
3	$(CA6)_s + (C)_l + (S)_l = (C2AS)_s + 5(A)_l$	328,603–213.14T	−1529	1.11
4	$(CA2)_s + (C)_l + (S)_l = (C2AS)_s + (A)_l$	−78,909–20449.01T	−110494	1.46E3
5	$(CA6)_s + (C)_l + 2(M)_l + 8(A)_l = (C2M2A14)_s$	-1E6+499.49T	−495875	1.61E14
6	$2(CA6)_s + 2(M)_l + 2(A)_l = (C2M2A14)_s$	−551,979 + 204.75T	−234741	5.31E6
7	$(A)_l + (M)_l = (MA)_s$	−115,132 + 26.59T	−542956	35.94
8	$(C2M2A14)_s + 2(M)l + 2(A)_l = 2(CM2A8)_s$	−442,000 + 144.61T	−105900	1.08E3
9	$(CA6)_s + 2(M)_l + 2(A)_l = (CM2A8)_s$	−496,990 + 174.68T	−226376	3.06E6
10	$(CM2A8)_s + 6(M)_l = 8(MA)_s + (C)_l$	−306,316 + 37.71T	−276388	8.29E7

C: CaO, A: Al_2O_3, S: SiO_2, M: MgO. The subscript s and l denote the solid and liquid state of the phases, respectively.

and form a continuous solid layer around the particle, as indicated from t_0 to t_2. This layer inhibits the transport of reactants and products, causing no boundary layer to form between the undissolved particle and the intermediate solid layer. However, a boundary layer formed between the bulk slag and the intermediate solid layer. Additionally, as shown in Fig. 12(c1), the formation of the intermediate solid layer significantly decreased the ΔC (C_{s1} - C_b) by altering the interface from slag – particle to slag – intermediate solid layer, significantly slowing the dissolution kinetics. CA2 particles [13] and CA6 particles dissolving in slag S3 followed this mechanism. The formation of this dense layer is also expected to reduce the effective diffusion coefficients of dissolving species due to lower ionic mobility through the solid reaction product layer. This added resistance to mass transport further contributes to the observed slowdown in dissolution kinetics.

Table 3
SEM-EDS point scan results along CA6 – slag S3 interface in Fig. 8(c).

Spectrum	Elemental Composition (wt.%)			Phases
	Ca	Al	Si	
1	32	11	17	slag S3
2	29	19	12	melilite
3	31	10	17	slag S3
4	29	17	13	melilite
5	28	20	11	melilite
6	29	20	11	melilite
7	4	38	16	mixture
8	16	41	1	CA2
9	14	24	18	mixture
10	28	20	11	melilite
11	15	40	2	CA2

Table 4
Elemental composition of CA6 particle, slags, and relevant intermediate solid products.

	Elemental composition (wt.%)			
	Ca	Al	Si	Mg
CA6	6	48	0	0
Slag S3	34	7	17	0
Slag S6	30	18	7	5
CA2	15	42	0	0
MA	0	38	0	17
C2AS	29	20	10	0
CM2A8	4	45	0	5

Table 5
SEM-EDS point scan results along CA6 particle – slag S6 interface in Fig. 10(c).

Spectrum	Elemental Composition (wt.%)				Phases
	Ca	Al	Si	Mg	
1	14	40	1	2	CA2
2	6	48	0	0	CA6
3	0	38	0	17	spinel
4	1	38	0	17	spinel
5	26	26	6	1	mixture
6	27	25	7	1	mixture
7	17	41	0	0	CA2
8	6	48	0	0	CA6
9	16	42	0	0	CA2
10	6	49	0	0	CA6
11	6	49	0	0	CA6
12	26	34	0	0	CA
13	29	21	6	4	slag S6
14	29	19	7	5	slag S6

3.5. *Practical viewpoint for the steelmaking process*

In steelmaking, a comprehensive understanding of the dissolution behavior of particles in steelmaking slags, particularly those formed as solid inclusions and used in refractories (e.g., CA2 and CA6), is crucial for enhancing steel cleanliness and extending refractory service life. To improve steel cleanliness, this study suggests that slags with a C/A ratio between 1 and 2, low SiO_2 content, and approximately 5 wt% MgO are preferred. This composition promotes particle dissolution via the direct dissolution mechanisms, enhancing refining efficiency. Conversely, to extend refractory longevity, the indirect dissolution mechanism is desirable for interactions between molten slag and refractories. For instance, high C/A ratio slags promote the formation of a continuous solid product layer, which acts as a diffusion barrier. This slows the dissolution process, and prevents contamination, thereby preserving refractory performance.

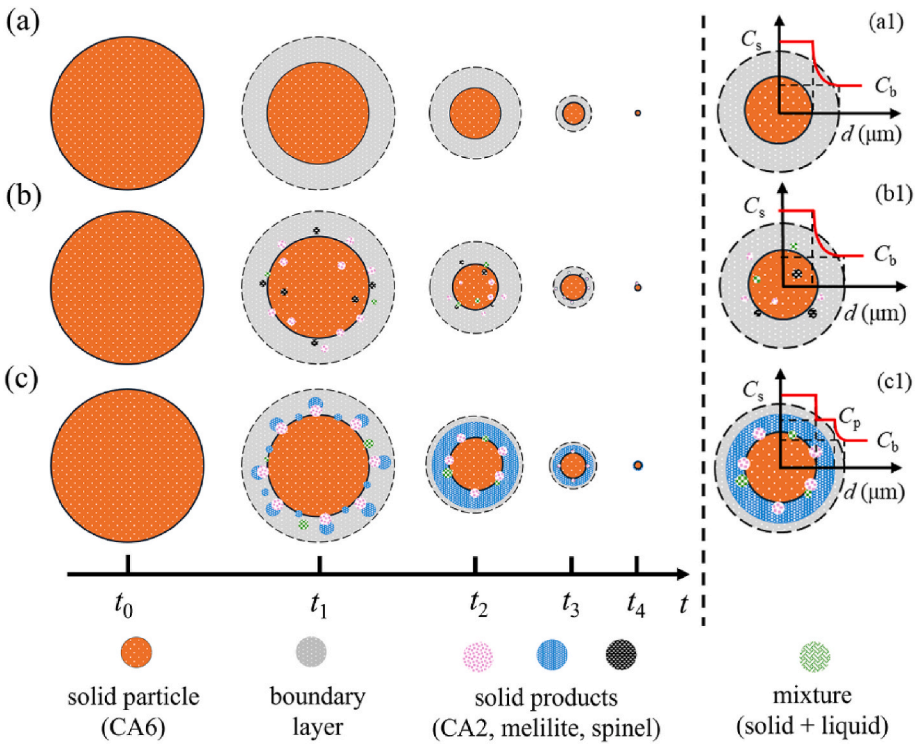

Fig. 12. Schematic diagram for dissolution mechanism of solid particles in molten slag (a) Direct dissolution without intermediate solid products formation, (b) Direct dissolution with formation of intermediate solid products, and (c) Indirect dissolution. (a1) - (c1) present the concentration profile of the dissolving species corresponding to these dissolution mechanisms (C_s, C_p, and C_b donate the concentration of the dissolving species at particle – slag interface, in the solid product, and in bulk slag, respectively.).

4. Conclusions

This study systematically investigated the impacts of slag C/A ratio and slag viscosity on the dissolution kinetics of CA6 and CA2 particles at 1550 °C in CaO-Al_2O_3-SiO_2-(MgO) metallurgical slags, utilizing HT-CLSM. Post-dissolution analysis through SEM-EDS and thermodynamic calculations provided insights into the dissolution path and mechanisms. Three distinct dissolution mechanisms were proposed based on these findings. The key conclusions are as follows:

(1) There are two distinct dissolution mechanisms of solid particles,
   (a) *Direct dissolution*: 1) No intermediate solid products form, and the dissolution kinetics are controlled by the mass transport of species through the boundary layer. The driving force ($\Delta C_{Al_2O_3}$) is constant. 2) Irregular dispersed intermediate solid products formed during the dissolution process due to the chemical reactions between the molten slag and the particle. However, they do not have an impact on the ΔC and do not retard the dissolution kinetics of the particle.
   (b) *Indirect dissolution with solid layer formation:* An intermediate solid layer forms around the particle, inhibiting the transport of species and reducing $\Delta C_{Al_2O_3}$ by altering the interface from slag – particle to slag – intermediate solid layer, significantly slowing dissolution kinetics.

(2) The impact of intermediate solid products on dissolution kinetics was strongly influenced by their morphology, whether they formed a solid layer or randomly dispersed intermediate solid particles. This morphological effect significantly influenced ΔC but was not fully captured in the thermodynamic modelling.

(3) An increase in the C/A ratio and a decrease in the viscosity of slag enhanced the dissolution rate of CA6 particles. However, it was observed the formation of a solid product layer (melilite) around the CA6 particle in slag with a C/A ratio of 3.8 acted as a hindrance, impeding its dissolution.

(4) The dissolution kinetics of CA2 and CA6 particles were improved with increased MgO content in slag.

CRediT authorship contribution statement

Guang Wang: Writing – review & editing, Writing – original draft, Methodology, Investigation, Formal analysis, Data curation, Conceptualization. **Muhammad Nabeel:** Writing – review & editing. **Neslihan Dogan:** Writing – review & editing, Supervision, Project administration, Funding acquisition. **Wangzhong Mu:** Writing – review & editing. **A.B. Phillion:** Writing – review & editing, Supervision, Project administration, Funding acquisition.

Declaration of competing interest

The authors declare that they have no known competing financial interests or personal relationships that could have appeared to influence the work reported in this paper.

Acknowledgments

The authors would like to thank the Natural Sciences and Engineering Research Council of Canada (NSERC) for funding this research. This research used a High Temperature Confocal Laser Scanning Microscopy-VL2000DX-SVF17SP funded by Canada Foundation for Innovation John Evans Leaders Fund (CFI JELF, Project Number: 32826), a scanning electron microscope JEOL 6610 located at the Canadian Centre for Electron Microscopy at McMaster University, and a PANalytical X'Pert diffraction instrument located at the Centre for crystal growth, Brockhouse Institute for Materials Research.

References

[1] Z.Y. Deng, M.Y. Zhu, Evolution mechanism of non-metallic inclusions in Al-killed alloyed steel during secondary refining process, ISIJ Int. 53 (2013) 450–458.
[2] L. Holappa, O. Wijk, Inclusion Engineering, 2014.
[3] S.K. Michelic, C. Bernhard, Significance of nonmetallic inclusions for the clogging phenomenon in continuous casting of Steel—A review, Steel Res. Int. 93 (2022) 1–18.
[4] R. Salomão, V.L. Ferreira, L.R. Oliveira, A.D. Souza, W.R. Correr, Mechanism of pore generation in calcium hexaluminate (CA6) ceramics formed in situ from calcined alumina and calcium carbonate aggregates, J. Eur. Ceram. Soc. 36 (2016) 4225–4235.
[5] L.P. Pan, Y.W. Li, F.G. Tan, Q. Wang, Y.C. Chen, Q.H. Wang, T.B. Zhu, N. Liao, Y. B. Xu, Influence of calcium hexaluminate gradation on interfacial microstructure and fracture behavior of cement-bonded alumina castables, Ceram. Int. 49 (2023) 16137–16148.
[6] M.A. Braulio, G.G. Morbioli, D.H. Milanez, V.C. Pandolfelli, Calcium aluminate cement source evaluation for Al2O3–MgO refractory castables, Ceram. Int. 37 (2011) 215–221.
[7] H. Zhang, Y.B. Peng, S. Zhang, C.S. Liu, R.J. Cheng, H.W. Ni, Effects of refining slag on transformation and removal of inclusions in type 430 stainless steel, Metall. Mater. Trans. B 53 (2022) 702–715.
[8] J.S. Li, Y. Sun, S.F. Yang, W. Liu, Research status of numerical simulation of nonmetallic inclusions interfacial removal, Steel Res. Int. 94 (2023) 1–19.
[9] M. Valdez, K. Prapakorn, A.W. Cramb, S. Sridhar, A study of the dissolution of Al2O3, MgO and MgAl2O4 particles in a CaO-Al2O3-SiO2 slag, Steel Res. Int. 72 (2001) 291–297.
[10] J. Liu, M. Guo, P.T. Jones, F. Verhaeghe, B. Blanpain, P. Wollants, In situ observation of the direct and indirect dissolution of MgO particles in CaO–Al2O3–SiO2-based slags, J. Eur. Ceram. Soc. 27 (2007) 1961–1972.
[11] G. Wang, M. Nabeel, N. Dogan, M. Abid, W.Z. Mu, A.B. Phillion, Impact of porosity and velocity on the dissolution behaviors of calcium aluminate inclusions in CaO-SiO2-Al2O3 steelmaking slag: in-situ observations and model advancements, Metall. Mater. Trans. B (2025) 1–13.
[12] K.Y. Miao, A. Haas, M. Sharma, W.Z. Mu, N. Dogan, In situ observation of calcium aluminate inclusions dissolution into steelmaking slag, Metall. Mater. Trans. B 49 (2018) 1612–1623.
[13] G. Wang, M. Nabeel, W.Z. Mu, A.B. Phillion, N. Dogan, In-situ confocal microscopy study on dissolution kinetics of calcium aluminate inclusions in CaO-Al2O3-SiO2 type steelmaking slags, J. Iron Steel Res. Int. 32 (2025) 364–375.
[14] B. Guo, J.J. Wang, L.F. Zhang, Dissolution kinetics of Al2O3, CaAl4O7, and MgAl2O4 inclusions into CaO–Al2O3–SiO2 slags with varying MgO content, Metall. Mater. Trans. B 56 (2024) 1025–1043.
[15] J.H. Park, I.H. Jung, H.G. Lee, Dissolution behavior of Al2O3 and MgO inclusions in the CaO–Al2O3–SiO2 slags: formation of ring-like structure of MgAl2O4 and Ca2SiO4 around MgO inclusions, ISIJ Int. 46 (2006) 1626–1634.
[16] X.L. Guo, J.V. Dyck, M.X. Guo, B. Blanpain, Phase evolution and nature of oxide dissolution in metallurgical slags, AIChE J. 59 (2013) 2907–2916.
[17] J. Li, E.A. Medina, J.K. Stalick, A.W. Sleight, M.A. Subramanian, Structural studies of CaAl12O19, SrAl12O19, La2/3+δ Al12–δO19, and CaAl10NiTiO19 with the hibonite structure; indications of an unusual type of ferroelectricity, Z. Naturforsch. B Chem. Sci. 71 (2016) 475–484.
[18] M. Lind, L. Holappa, Transformation of alumina inclusions by calcium treatment, Metall. Mater. Trans. B 41 (2010) 359–366.
[19] C.W. Bale, E. Bélisle, P. Chartrand, S.A. Decterov, G. Eriksson, A.E. Gheribi, K. Hack, I.H. Jung, Y.B. Kang, J. Melançon, A.D. Pelton, S. Petersen, C. Robelin, J. Sangster, P. Spencer, M.A. Ende, Reprint of: factsage thermochemical software and databases, 2010–2016, Calphad 55 (2016) 1–19.
[20] G. Urbain, Viscosité et structure de silicoalumineux liquides, Rev. Int. Hautes Temp. Refract. 2 (1974) 133–145.
[21] H. Chikama, H. Shibata, T. EmIand, M. Suzuk, "In-situ" real time observation of planar to cellular and cellular to dendritic transition of crystals growing in Fe–C alloy melts, Mater. Trans. JIM 37 (1996) 620–626.
[22] C. Orrling, Y. Fang, N. Phinichka, S. Sridhar, A.W. Cramb, Observing and measuring solidification phenomena at high temperatures, JOM-e 51 (1999) 1–5.
[23] C.A. Schneider, W.S. Rasband, K.W. Eliceiri, NIH image to ImageJ: 25 years of image analysis, Nat. Methods 9 (2012) 671–675.
[24] X.L. Guo, Z.H.I. Sun, J.V. Dyck, M.X. Guo, B. Blanpain, In situ observation on lime dissolution in molten metallurgical slags–Kinetic aspects, Ind. Eng. Chem. Res. 53 (2014) 6325–6333.
[25] V.D. Eisenhüttenleute, Slag Atlas, 2ed Edition ed., Verlag Stahleisen GmbH, Düsseldorf, 1995.
[26] D.R. Gaskell, The thermodynamic properties and structures of slags, Metall. Treatises 6 (1981) 59–78.
[27] M. Sajid, C.G. Bai, M. Aamir, Z.X. You, Z.M. Yan, X.X.M. Lv, Understanding the structure and structural effects on the properties of blast furnace slag (BFS), ISIJ Int. 59 (2019) 1153–1166.
[28] Z. Deng, X. Zhang, G. Hao, C. Wei, M. Zhu, Dissolution behavior of Al2O3 inclusions into CaO–MgO–SiO2–Al2O3–TiO2 system ladle slags, Int. J. Miner. Metall. Mater. 31 (2024) 977–987.